THE JOURNAL OF PHYSICAL CHEMISTRY C

Article

Promotion Effects in the Oxidation of CO over Zeolite-Supported Rh Nanoparticles

Muriel Lepage, Tom Visser, Fouad Soulimani, Andrew M. Beale, Ana Iglesias-Juez, Ad M. J. van der Eerden, and Bert M. Weckhuysen

J. Phys. Chem. C, **2008**, 112 (25), 9394-9404 • DOI: 10.1021/jp711743g • Publication Date (Web): 29 May 2008

Promotion Effects in the Oxidation of CO over Zeolite-Supported Rh Nanoparticles

Muriel Lepage,[†,‡] Tom Visser,[‡] Fouad Soulimani,[‡] Andrew M. Beale,[‡] Ana Iglesias-Juez,[‡] Ad M. J. van der Eerden,[‡] and Bert M. Weckhuysen*[,‡]

Advanced Technology Division, Toyota Motor Europe, Hoge Wei 33B, 1930 Zaventem, Belgium, and Inorganic Chemistry and Catalysis Group, Department of Chemistry, Utrecht University, Sorbonnelaan 16, 3584 CA Utrecht, The Netherlands

Received: December 14, 2007; Revised Manuscript Received: March 1, 2008

Rh particles with an average diameter smaller than 1.5 nm have been supported on a series of zeolite Y samples. These zeolite materials contained different monovalent (H^+, Na^+, K^+, Rb^+, and Cs^+) and divalent (Mg^{2+}, Ca^{2+}, Sr^{2+}, and Ba^{2+}) cations and were used as model systems to investigate the effect of promoter elements in the oxidation of CO over supported Rh particles in excess of oxygen. Infrared (IR) spectroscopy was carried out to monitor the electronic changes in the local environment of Rh-adsorbed CO. It was found that the bands corresponding to two Rh *gem*-dicarbonyl species, $Rh^+(CO)_2-(O_z)_2$ and $Rh^+(CO)_2-(O_z)(H_2O)$, shift to lower wavenumbers with increasing ionic radius/charge ratio of the cation. In addition, the relative intensity of the bridge bonded CO as compared to the total absorbance of Rh-bonded CO species decreases with increasing Lewis acidity, as expressed by the Kamlet−Taft parameter α of the cation. This trend could be directly correlated to the Rh CO oxidation activity, since low temperatures at 50% CO conversion corresponded with catalyst materials with a high contribution of bridge-bonded CO species and hence with small α values. A lower Lewis acidity causes an increased electron density on the framework oxygen atoms and thus an increased electron density on the zeolite-supported Rh particles. Comparable trends have been observed previously on a similar series of cation containing zeolite supported Pt catalyst materials.

Introduction

The catalytic activity of supported nanometer-size metal particles is generally recognized to be influenced by the chemical composition of support materials due to weak, medium, or strong metal−support interactions. Among these supported metal catalysts, Rh plays an important role due to its versatile catalytic behavior. For example, Rh supported on zeolites has been investigated for the hydroformylation of alkenes,[1] the hydrogenation of arenes, CO or CO_2,[2] the carbonylation of methanol,[3] and the conversion of synthesis gas into hydrocarbons or oxygenates.[4] However, its best known application is in the three-way exhaust automotive catalyst, where it is used for its capacity to reduce NO_x in excess of oxygen to a higher level than Pd or Pt.[5] In this specific system, the support is usually a complex mixture of metal oxides (e.g., Al_2O_3, SiO_2, ZrO_2, and CeO_2) and promoters (e.g., Ba, K and La). Several studies have shown that these supports influence the Rh metal dispersion as well as its reducibility. It was also shown by the groups of Mariadassou[6,7] and Yu Yao[8] that these Rh properties directly influence the type of kinetics taking place on the Rh active sites during the oxidation of CO.

The goal of this work is to elucidate Rh−support interactions in a systematic manner by studying Rh-based model catalysts making use of zeolites as supports in which different monovalent (H^+, Na^+, K^+, Rb^+, and Cs^+) and divalent (Mg^{2+}, Ca^{2+}, Sr^{2+}, and Ba^{2+}) cations are present. The leading idea, inspired by our previous work on zeolite-supported Pt nanoparticles,[9–11] is that the electronic properties and related CO oxidation activity behavior of Rh particles encaged in zeolite Y would be influenced by promoter elements added to the support material. By using CO as a probe molecule in combination with infrared spectroscopy, it will be shown that an increasing electron density on the supported Rh nanoparticles, indirectly induced by alkaline and earth alkaline metal ions via the framework oxygen atoms, promotes the CO oxidation activity. The work therefore provides guidelines for the development of improved three-way exhaust catalytic converters containing lower amounts of noble metals.

Experimental Methods

Prior to preparation and characterization, it should be emphasized that the CO stretching vibration of Rh-chemisorbed CO is not only sensitive to the support characteristics, but also to a large number of experimental parameters. According to literature, the loading, dispersion, particle size, and coordination number of Rh, its precursor, the reduction temperature, and CO exposure pressure can affect the observed IR data, whereas sample pretreatment, CO exposure temperature, CO adsorption, and CO interaction with support cations may play a role as well.[12–20] To prevent erroneous assignments and conclusions, special attention has been paid to keep the experimental parameters and the instrumental settings as far as possible identical.

1. Catalyst Preparation. The starting material for ion exchange was a Na−Y material from AKZO Nobel with a Si:Al ratio of 2.3. The zeolite support materials with H^+, K^+, Rb^+, Cs^+, Mg^{2+}, Ca^{2+}, Sr^{2+}, and Ba^{2+} were obtained by five consecutive ion exchanges for 24 h with an aqueous 0.1 M solution of NH_4NO_3 (Acros, p.a.), KCl (Acros, p.a.), RbCl (Acros, 99+ %), CsCl (Acros, 99+ %), $MgCl_2$ (Acros, p.a.), $CaCl_2$ (Aldrich, 98+ %), $SrCl_2$ (Acros, 99.99%), and $BaCl_2$ (Aldrich, 99.999%), respectively. The pH of the solution was

* To whom correspondence should be addressed. Phone: +31-30-2534328. Fax: +31-30-2511027. E-mail: b.m.weckhuysen@uu.nl.
† Toyota Motor Europe.
‡ Utrecht University.

10.1021/jp711743g CCC: $40.75
Published on Web 05/29/2008

kept between 6.5 and 7.5, and the zeolite material was separated from the solution through centrifugation for 30 min at 4000 rpm. The samples were then washed chlorine-free with deionized water, which was examined with $AgNO_3$, before being dried at 323 K for 48 h. The crystallinity, before and after ion exchange, was verified by X-Ray diffraction (XRD) on the Rh/RbY sample as a method check that the ion exchange method does not modify the crystalline structure of the zeolite support.[9]

Before impregnation, the support was dried under vacuum at 473 K for 2 h. $RhCl_3 \cdot 2H_2O$ (Alfa, 99.9%) was chosen as the precursor and incipient wetness as the impregnation method. In this combination, the Rh ion complex is small enough to enter the zeolite channel and it minimizes a decrease in the concentration of the charge compensating ion.[18] The target Rh loading was 0.5 wt %. The concentration of the precursor solution was calculated taking into account the change in material density caused by the introduction of the cations. After impregnation, the powder was dried for 12 h at room temperature and for 8 h at 353 K in an oil bath under flowing N_2 (quality 4.0; Linde). It was then pressed at 8 Tons, grinded, and sieved to pellets of 212−425 μm diameter. The calcination was carried out in a tubular reactor in a high air flow (1335 mL/min). The temperature was first increased to 423 K at a rate of 5 K/min, where it was kept for 8 h, and then further to 573 K at a rate of 0.2 K/min where it was maintained for 1 h. Following cooling, the pellets were reduced in a H_2 (quality 5.0; Linde) flow (380 mL/min) at 573 K for 2 h after a temperature ramp-up of 5 K/min. Finally, the Rh particles were stabilized by a short surface reoxidation at room temperature to prevent agglomeration.

2. Catalyst Characterization. Rh and cation loadings of the samples were determined making use of atomic emission spectroscopy (AES) with an inductively-coupled plasma (ICP) as atomization source on a Shimadzu ICPS-8100 machine. For this purpose, the catalysts were dissolved in a mixture of hydrofluoric, nitric, and hydrochloric acids.

High resolution transmission electron microscopy (HR-TEM) was performed with a Philips CM 30 UT electron microscope equipped with a field emission gun as the electron source operated at 300 kV. Samples were mounted on a microgrid made of carbon polymer supported on a copper mesh by placing a few droplets of a suspension of ground sample in ethanol on the grid, followed by drying at ambient conditions. Based on the TEM pictures, the particle size distribution for all particles larger than 1 nm was evaluated by using the analySIS software (Philips). The size distribution was calculated on the basis of the average diameter of at least 150 particles found on one TEM picture. In order to verify the consistency of this methodology, two different TEM pictures from the same sample were analyzed, and very similar results for both the average particle size and the standard deviation were obtained. In the same way, we also confirmed that the Rh nanoparticles were not sintering during the heat treatments, i.e., throughout the reduction, evacuation, and temperature programmed desorption processes.

Extended X-ray absorption fine structure (EXAFS) measurements were carried out in the CRG DUBBLE (BM26A) beamline at the ESRF synchrotron (Grenoble, France). The beamline was equipped with a double Si(111) crystal monochromator. Measurements were performed in transmission mode, and ion chambers were used for detection with a gas fill to absorb 20% in the first and 80% in the second ion chamber. Reduction of the higher harmonic radiation was established using a vertically focusing Pt/Si mirror installed behind the monochromator. The samples were prepared by hand pressing 0.5 g of powder into a self-supporting wafer. This wafer was then placed in a treatment cell and reduced in a flow of 10% H_2 in He for 15 min at 423 K and for 30 min at 573 or 623 K, the temperature ramp-up rate being 5 K/min. Afterward, the cell was evacuated for 30 min at 573 K before being measured under active vacuum at liquid-N_2 temperature. Each measurement was repeated two times at the Rh K edge. The EXAFS data analysis was carried out with the XDAP program.[21] The EXAFS data was extracted from the averaged absorption spectra through pre-edge subtraction using a modified Victoreen curve and then through background subtraction employing cubic spline routines with a continuously adjustable smoothing factor. Finally, the average spectrum was normalized by dividing the data by the absorption intensity at 50 eV after the edge.[22] The obtained chi (χ) function was analyzed by multiple shells data fitting in the k space with a k^3 weighting. The reliability of the fitted parameters was then verified with the goodness of fit for the k^1 weighted χ function. References were created for the phase-shifts and backscattering amplitudes corrections of Rh−Rh, Rh−Cl, and Rh−O contributions based on experimental absorption spectra measured on a Rh foil (Aldrich, 12 μm thick, 99.9%) and on $RhCl_3 \cdot 2H_2O$ (Aldrich, 98%) and Rh_2O_3 (Aldrich, 99.8%). The obtained Rh−Rh coordination numbers were used to evaluate the average Rh particle size.

IR measurements were performed on self-supporting catalyst wafers that were pressed from 0.01 to 0.02 g of the passivated and finely grained sample material. A pressure of no more than 3 bar was applied during 10 s to prevent destruction of the pore structure of the support. The wafer was placed in an IR transmission cell equipped with CaF_2 windows. The cell was evacuated to 2×10^{-8} bar at 323 K for at least 1 h prior to reduction by a 40−60 mL/min flow of H_2 (quality 5.0; Linde). During reduction, the temperature was raised from 323 to 573 K at 3 K/min; it was maintained for 1 h at 573 K. The system was then switched back to vacuum for 1 h at 573 K, before being cooled down to 323 K at a rate of 3 K/min. A first spectrum was taken under vacuum and served as background reference for the catalyst wafer. Next, 10% CO (quality 2.0; Linde) in He (quality 4.6; Linde) was introduced in the cell until a stable pressure of ca. 0.06 bar was reached. After 30 min of static CO exposure, the cell was evacuated to a pressure of 2×10^{-6} bar for 30 min at 323 K before the temperature programmed desorption (TPD) was started by increasing the temperature up to 573 K at a rate of 3 K/min. IR spectra were recorded every 2 min on a Perkin-Elmer 2000 FTIR instrument with a data point resolution of 4 cm^{-1} and an accumulation of 25 scans with wavenumbers ranging from 4000 to 1300 cm^{-1}. The data acquisition was performed automatically using the Perkin-Elmer TimeBase software. The reproducibility of all IR-TPD measurements was verified by repeating the experiments in two ways: (1) on two different wafers from the same sample and (2) on the same wafer by applying the same procedure two times in a row without opening the IR cell. Band positions and corresponding intensity data were estimated by peak fitting of the baseline corrected spectra using the Grams AI software. After evaluation of the different peak profiles, it was concluded that the Voigt profile was giving the best fits for well-defined maxima as well as for shoulders. Each spectrum was fitted with 7−8 Voigt-type peaks depending on its shape in the 2200−1550 cm^{-1} wavenumbers range. It should be noted that the peak positions obtained were very consistent, while repeating the fitting with different starting conditions. The same is valid for the integrated intensity of the peaks situated between 2200 and 2020 cm^{-1}. The broad and overlapping peaks below

TABLE 1: Summary of the Synthesized Model Catalysts and Their Main Characteristics

	ICP-AES		TEM		EXAFS	
Rh/M^{n+}Y	Na^+ exchange [%]	Rh [wt %]	particle size [nm]	Average particle size [nm]	Rh−Rh coordination number	average particle size [nm][a]
Rh/HY	NA	0.21	<5	2.5	7.0	∼1.3
Rh/NaY	100	0.33	<6	3.1	6.5	∼1.2
Rh/KY	78	0.32	<5	2.7	6.3	∼1.1
Rh/RbY	65	0.36	<3	1.3[b]	5.8	∼1.0
Rh/CsY	72	0.49	<6	2.6	6.4	∼1.1
Rh/MgY	66	0.32	<4	2.2	5.0	∼0.9
Rh/CaY	77	0.38	<6	2.7	6.1	∼1.1
Rh/SrY	83	0.39	<3	1.9	1.8[c]	<0.6
Rh/BaY	83	0.45	<4	1.5	3.7	∼0.7

[a] Average particle size based on the work done by van Zon et al.[28] and by Gloor and Prins.[29] [b] The TEM pictures of this sample were much better, which allowed us to see smaller particles and gives a lower average particle size. [c] The fit on this sample was not as good as on the others. The magnitude of the EXAFS Fourier Transform around 2.69 Å was however very similar to the one obtained on Rh/BaY, which points to comparable Rh particle sizes.

2020 cm^{-1} hampered evaluation of the integrated areas of the individual components with great precision.

3. Catalytic Testing. The zeolite-based Rh catalysts were tested for the oxidation of CO in a U-tube reactor equipped with a thermocouple placed in the catalytic bed, a furnace, and mass flow controllers. For this purpose, 20 mg of each catalyst diluted with 200 mg of SiC was loaded in the reactor. The reacting gas consisted of 2000 ppm of CO (10% CO, quality 2.0; in He, quality 4.6; Linde) in 10% of O_2 (quality 5.0; Linde) and N_2 (quality 4.0; Linde) as balance. The total flow rate was 100 mL/min, and the heating rate was 5 K/min. The CO conversion was calculated between 278 and 773 K from FT-IR spectra measured every 25−35 s in a transmission flow cell using a Midac M2000 FT-IR spectrometer in the range of 2700−1985 cm^{-1} accumulating 4 scans at a resolution of 4 cm^{-1}.

Results and Discussion

1. Catalysts Characterization. First, the results from ICP-AES, EXAFS, and HR-TEM were evaluated to determine the Rh particle size, distribution, and loading as well as the rate of cation exchange of the zeolite support. The data have been summarized in Tables 1 and 2. In addition, a selection of TEM pictures with corresponding particle size distributions are presented in Figure 1.

The results of the ICP-AES analysis (Table 1) revealed that the amount of Rh in the different zeolite samples varies between 0.2 and 0.5 wt%, whereas the percentage of support Na^+ ions exchanged by $1/n$ M^{n+} ions reaches 65−83%. The latter values are not as high as the 98% ion exchange ratios reported in our previous work for Pt-based zeolites[9,23] but in line with the results of Kamble and co-workers.[24] As illustrated by the TEM data of Rh/HY, Rh/CsY, and Rh/KY in Figure 1, it was not possible to exclusively obtain Rh particles smaller than 1 nm. On the other hand, the particle size distribution graphs indicate that the Rh dispersion is about the same for all samples with an average particle diameter of 1.3−3.1 nm (Table 1). Furthermore, comparison of panels c and d in Figure 1 leads to the conclusion that sintering of the Rh nanoparticles did not take place during the heat treatments applied in the reduction and the TPD.

The Rh−Rh coordination numbers (N) obtained through EXAFS data analysis (Table 1) point to an average particle size in the range 0.7−1.3 nm, which is significantly smaller than the values derived from TEM. This virtual discrepancy between the results of both techniques is a well-known phenomenon, observed on various catalytic systems.[20,25,26] Jentys demonstrated that, in case the particles are small (i.e., $N < 10.5$), the EXAFS technique is more reliable than TEM or XRD.[27] Therefore, we conclude that most of the supported Rh particles are smaller than 1 nm and mainly located in the zeolite supercages.

TABLE 2: EXAFS Fitting Parameters Obtained in the k Range, with a k^3 Weighting[a]

Rh/M^{n+}Y	contribution	N	DW [Å^2]	R [Å]	E_0 [eV]	k range[b]
Rh/HY	Rh−Rh	7.0	0.0015	2.67	11.4	4.06−15.26
Rh/NaY	Rh−Rh	6.5	0.0044	2.64	6.6	4.23−14.04
	Rh−Cl	0.4	0.0000	2.36	1.8	
Rh/KY	Rh−Rh	6.3	0.0035	2.64	9.3	4.14−14.56
	Rh−Cl	0.5	0.0000	2.42	−5.0	
Rh/RbY	Rh−Rh	5.8	0.0030	2.64	7.8	4.17−14.70
	Rh−Cl	0.5	0.0000	2.42	−3.4	
Rh/CsY	Rh−Rh	6.4	0.0018	2.66	4.5	4.24−15.33
Rh/MgY	Rh−Rh	5.0	0.0034	2.66	5.3	4.15−15.30
Rh/CaY	Rh−Rh	6.1	0.0016	2.67	6.2	4.19−15.70
Rh/SrY	Rh−Rh	1.8	0.0008	2.66	9.0	4.04−13.92
	Rh−O	3.0	0.0000	2.75	−0.4	
Rh/BaY	Rh−Rh	3.7	0.0040	2.66	7.6	4.10−14.59
	Rh−O	2.2	0.0000	2.76	−5.1	

[a] N is the first shell coordination number, DW is the Debye Waller factor, R is the bond distance, and E_0 is the energy shift compared to the reference compounds. Typical errors are of the order of 10% for the Rh−Rh coordination numbers and 20% for the Rh−O and Rh−Cl ones, 5% for the Debye Waller factors, and 1−2% for the bond distances and 10% for the energy shifts.[22,27] [b] The k range was chosen to match nodes of the χ function.

Detailed analysis of the EXAFS spectra (Table 2) revealed, next to the main absorption signal from the first Rh−Rh shell, some small Rh contributions, which may originate from oxygen or chlorine.[28,29] In order to properly identify and quantify them, the difference file technique was applied.[22,28,30] This method started with the removal of the first Rh−Rh shell contribution from the χ function. Next, the sign of the imaginary part of the residual signal was examined after phase correction, using Rh_2O_3 and $RhCl_3$ as references for comparison. This is illustrated by Figure 2 for the Rh/NaY sample, where the imaginary part after subtraction of the Rh−Rh contribution and correction for the Rh−Cl phase showed a positive maximum between 2.2 and 2.5 Å confirming that there is some chlorine interacting with Rh. However, regarding the small coordination number of 0.5 (Table 2) as compared to the one of the precursor salt, i.e., 6, we conclude that its amount is small. Similar results were observed on the Rh/KY and Rh/RbY, whereas for all other samples, the remaining signal was too weak to extract reliable information on the chlorine scatterer. The slight asymmetry in the difference

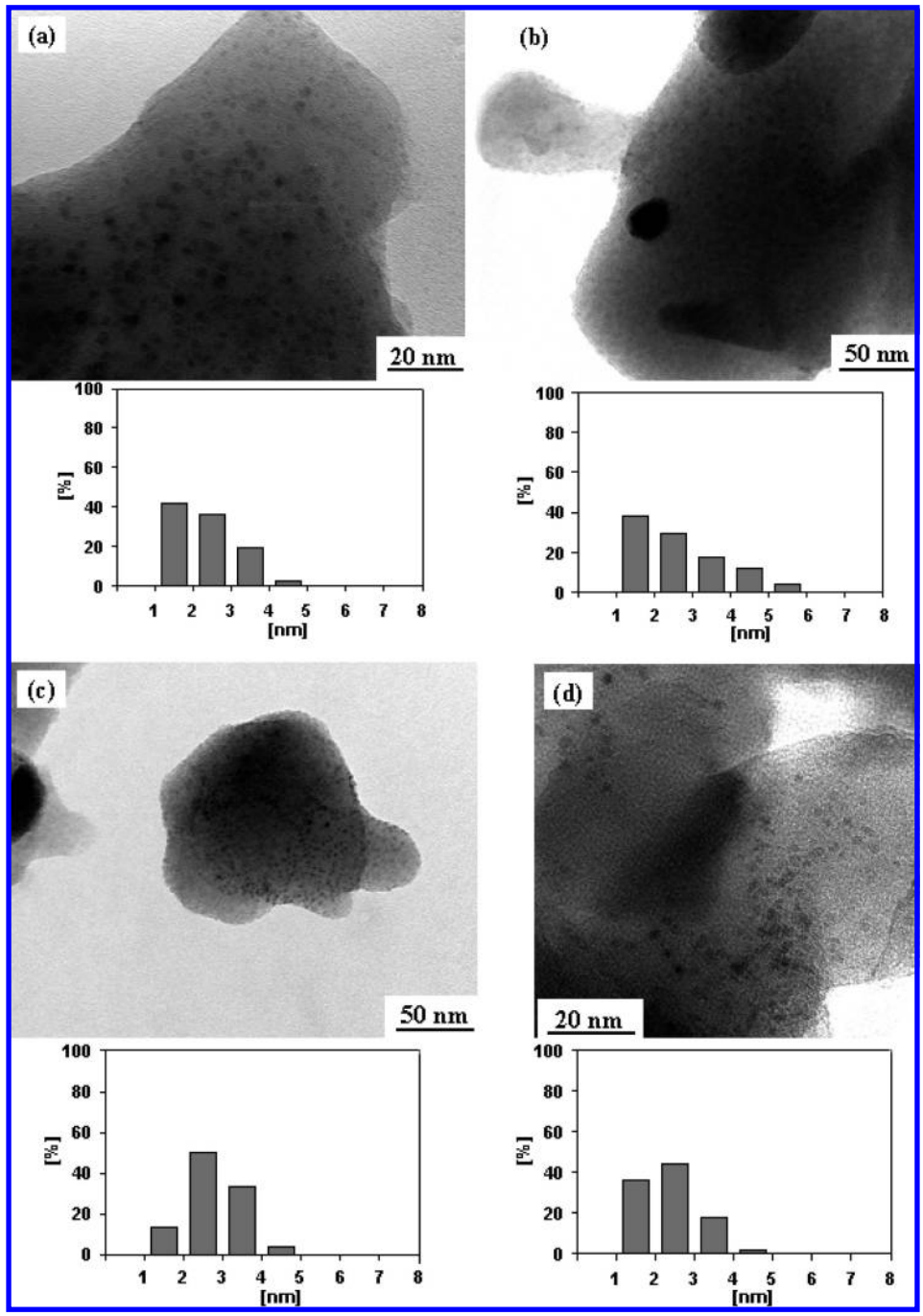

Figure 1. TEM pictures and their corresponding particle size distributions based on 150 particles, the ones smaller than 1 nm being excluded. Pictures have been taken on samples as prepared, (a) Rh/HY, (b) Rh/CsY, and (c) Rh/KY, and on a sample after CO exposure and temperature programmed desorption, (d) Rh/KY.

signal (as highlighted by the arrows in Figure 2) shows that oxygen scatterers also contribute to this signal. This contribution could only be fitted on the two samples with the smallest average particle size (i.e., Rh/SrY and Rh/BaY). There are two possible sources for this oxygen-Rh interaction:[19,29] (a) oxygen from the support at a distance varying between 2.5 and 2.8 Å, termed "long oxygen", or (b) oxidized Rh with a Rh−O bond length between 2.1 and 2.2 Å, being called "short oxygen". Assuming that our samples have been fully reduced before EXAFS measurement, it is expected that the main portion comes from long oxygen neighbors. However, the presence of Rh oxide in the analyzed samples after reduction cannot be totally excluded from the difference file signal. Moreover, it has been shown that it is difficult to fully reduce Rh on certain types of support oxides, such as alumina, ceria, zirconia and zeolites.[6–8,20,31–33] particularly, when the particles are very small and hence strongly interacting with the support.[6,34,35]

It should also be emphasized that the Rh−Rh bonding distances found are all shorter than the one obtained in a Rh crystal. This is in agreement with the contractions observed on small particles measured under vacuum conditions.[20,25,26,36,37] Finally, the Rh−Cl bonding distances appear a little long (ranging from 2.36 Å in Rh/NaY to 2.42 Å in Rh/KY and Rh/RbY) compared to the Rh−Cl bond distance in $RhCl_3$, which is 2.31 Å, or in $[Rh(CO)_2Cl]_2$ where bonds of 2.33 and 2.38 Å have been found.[28,30] It has however been shown that, after reduction, chlorine tends to stay on the Rh on silica supports but migrates away from the Rh surface on alumina supports.

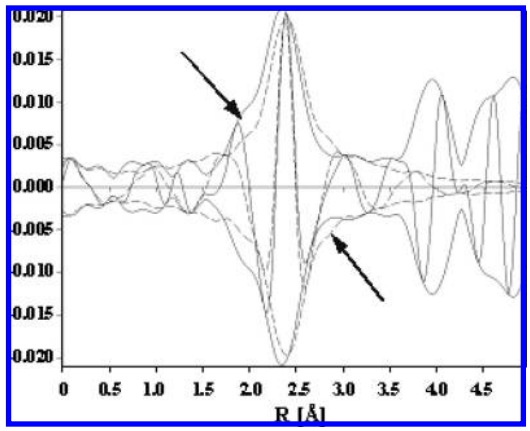

Figure 2. k^1 weighted Fourier transform of the EXAFS signal obtained on the Rh/NaY sample after removal of the Rh−Rh contributions and phase correction against the $RhCl_3$ reference (full line) and its corresponding fitted Rh−Cl contribution (dashed line).

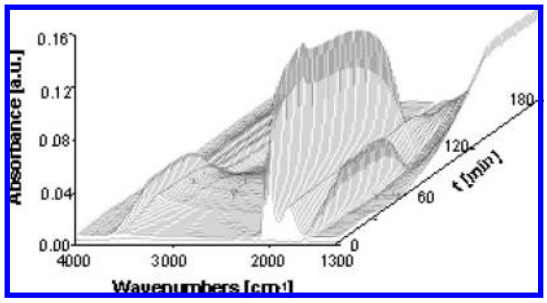

Figure 3. CO IR spectra measured during 30 min exposure to 0.06 bar CO, followed by 30 min vacuum at 323 K and temperature programmed desorption from 323 to 573 K at 3 K/min on Rh/CsY. Each spectrum is separated from the previous one by 2 min.

Since our samples have a Si:Al ratio of 2.7, it suggests a situation in between.[30,32] A last striking point comes from the Debye−Waller factors for the light scatterers, which are equal to zero. Nevertheless, such values have also been reported by other groups.[28,30]

2. Infrared Spectroscopy. The changes in the IR spectra, observed during the CO TPD experiments are illustrated by the time-resolved graph in Figure 3 for the catalyst Rh/CsY. Each spectrum is separated from the next one by 2 min. Upon exposure to CO ($t = 2$ min), absorption bands of Rh-bonded CO species immediately show up between 2150 and 1700 cm^{-1}, next to the CO gas phase band at 2143 cm^{-1}. All Rh-CO bands reach their maximum after 5−10 min and remain constant in position and intensity during exposure and vacuum treatment ($t = 30$−60 min). In time, bands also slowly grow in around 1640 and 3400 cm^{-1}, which start to disappear at about 400 K during TPD ($t = 85$ min). In accordance with Lefevbre et al.,[38] we assign these bands to traces of water adsorbed on the zeolite support. This was confirmed by additional IR experiments, where the bare support material was reduced, exposed to CO and subsequently submitted to TPD. The IR spectra obtained, revealed that the water bands originate from a slow diffusion of water into the cell during CO exposure since the same time-resolved spectral pattern was obtained, but without the presence of CO bands. It also implies that the occurrence of dehydroxylation reactions of the support[24] or the formation of carbonates[24,39–42] can be excluded. Further exposure of the wafers to various pressure levels of ambient air revealed that the diffusion under the normal experimental conditions was very small. Moreover, it turned out that the Rh−CO band positions and intensities are not affected at those low diffusion levels.

As illustrated by the time-resolved IR graphs of Rh/HY, Rh/NaY, Rh/CsY, and Rh/BaY in Figure 4, the catalysts not only exhibit clearly different band patterns but also a different behavior upon TPD. Except for Rh/HY, CO appears to be fully desorbed from the samples of the Rh/M^+Y series before the temperature of 573 K was reached. On the contrary, there is still CO adsorbed on the samples of the Rh/M^{2+}Y series at this temperature.

Prior to desorption, all catalysts show relatively sharp absorption bands in the range 2150−1900 cm^{-1} and a much broader pattern in the region 1900−1700 cm^{-1}. The former are generally attributed to linear Rh-bonded CO vibrations and the latter to bridge Rh-coordinated CO. The presence of both types of species in Rh supported on macroporous materials[6,12,13,15–17,31,33,34,43–52] and zeolites[16,17,19,32,53] has been widely reported.

The Region 1900−1700 cm^{-1}. As can be seen from Figure 4, the bandwidth, symmetry, and relative absorption intensity of the bridge-bonded CO band differ significantly depending on the cation of the support material. For Rh/HY (Figure 4a) and the Rh/M^{2+}Y series (e.g., Rh/BaY in Figure 4d), the band is less intense and broader, whereas for the latter ones, the asymmetry points to at least two different types of bridge Rh-coordinated CO species. It is commonly known, that the position and shape of the corresponding bands may change as a function of parameters such as the Rh loading, particle size, dispersion, and the type of support. It follows, that overlapping bands can originate from a CO bridge bonded to for instance two different Rh crystal faces or to small Rh clusters of different sizes. Finally, referring to literature, it is concluded that the absence of a separate band maximum around 1900−1920 cm^{-1} is in line with the EXAFS data, pointing to the presence of mainly small particles with an average diameter less than 1.5 nm.

The Region 2150−1900 cm^{-1}. It is evident from Figure 4 that several peaks contribute to the CO absorption pattern in the region 2150−1900 cm^{-1}. This is particularly clear in the spectra of Rh/NaY (Figure 4b) where at least five different contributions can be distinguished. Alongside the narrow peaks around 2100 and 2040 cm^{-1}, a broad absorption band appears to be overlapping at about 2000 cm^{-1}. On the basis of the position and width of this band, as well as on the fact that it disappears if the sample is oxidized in an oxygen flow for 1 h at 573 K, it can be concluded that the band corresponds to CO adsorbed in a bridge position on slightly oxidized Rh particles, where the Rh oxidation state lies between 0 and +1.[6,44,45] The presence of the latter is not an uncommon phenomenon in supported Rh catalysts even after calcination and reduction.[6,31,34,35,44]

Closer examination of the sharp bands between 2150 and 2000 cm^{-1}, revealed that four resolved bands are present for all samples except for the Rh/CsY catalyst (Figure 4c). Furthermore, the relative intensities varied considerably, depending on the cation introduced in the zeolite support material. Literature is not uniform in the assignment of the different peaks. For Rh supported on zeolite NaY, all authors reported the presence of two types of *gem*-dicarbonyls giving rise to 4 IR bands with maxima in the range 2118−2020 cm^{-1}.[16–20,38] The respective band positions for this catalyst are in good agreement with what we observe. The literature on Rh on other supports, such as alumina, silica, ceria, zirconia, titania, and other types of zeolites also describes the presence of a *gem*-dicarbonyl structure, i.e., $Rh^+(CO)_2$. This species is formed when small Rh particles are exposed to CO, through the disruption of the small Rh metal clusters into isolated Rh cations with the participation of

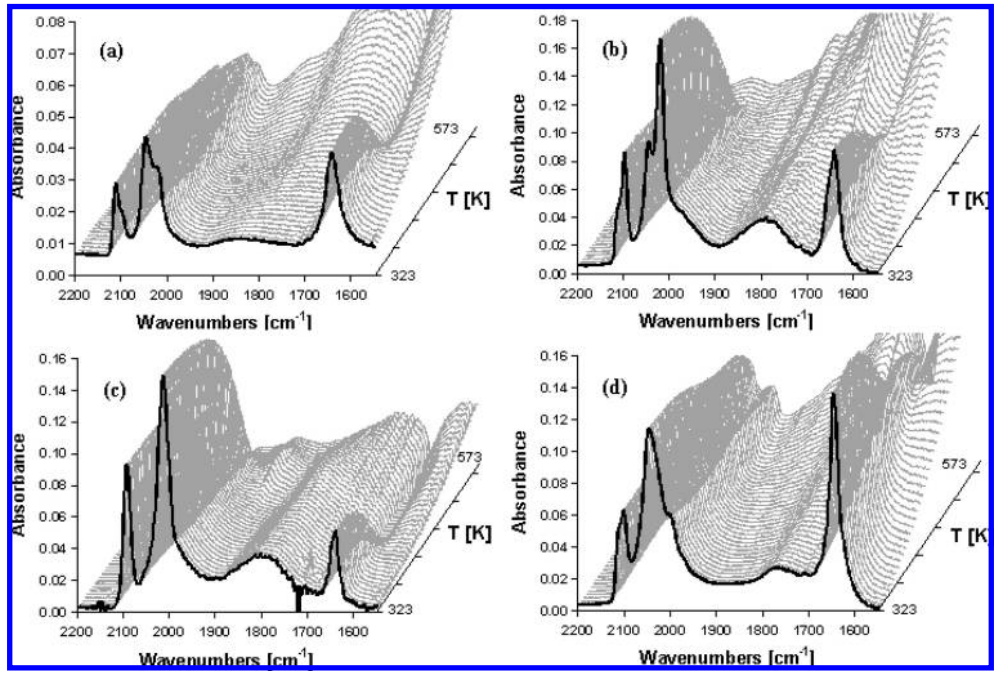

Figure 4. CO IR spectra after 30 min exposure to 0.06 bar CO and 30 min vacuum at 323 K during the temperature programmed desorption from 323 to 573 K obtained on (a) Rh/HY, (b) Rh/NaY, (c) Rh/CsY, and (d) Rh/BaY samples. Each spectrum is separated from the previous one by 2 min or 6 K.

the OH groups of the support.[16,54] It results in two bands in the CO IR spectrum: one in-phase CO stretching vibration between 2118 and 2070 cm^{-1} and one out-of-phase stretching vibration between 2053 and 2007 cm^{-1}.[6,12–18,30,31,33–35,43–46,48–56] Next to these, linearly bonded CO adsorbed on Rh metallic particles has been reported to give rise to a band between 2075 and 2031 cm^{-1}, whereas CO linearly adsorbed on oxidized Rh^{1+} or Rh^{2+} crystallites is attended with a band between 2135 and 2110 cm^{-1}.[6,12,15–17,19,32–34,43–51,53] In order to unambiguously assign the four bands observed in the spectra of our catalysts, two additional tests have been performed (data not shown for brevity).

In the first experiment, the Rh/NaY sample was oxidized in air for 1 h at 573 K and then measured in the IR cell following the procedure described above except for the reduction step. Comparison of the CO IR spectra obtained on the reduced and oxidized catalyst highlighted that a band at 2134 cm^{-1} showed up. It can be associated to CO linearly bonded to Rh^{2+} or Rh^{3+}.[16,18,20,44,45,53] Furthermore, the absorption intensity around 2070 cm^{-1} (linear CO on Rh^0) and below 1950 cm^{-1} (bridged CO) was reduced, whereas the *gem*-dicarbonyl bands at around 2100 and 2000 cm^{-1} were unchanged in intensity and position. In the second experiment, the CO gas was introduced in the cell on the reduced Rh/NaY sample at liquid-nitrogen temperature. Next to the intense peak of the linear CO on Rh^0, two broad bands showed up at 1980 and 1800 cm^{-1} that can be easily attributed to CO bridge bonded to oxidized and metallic Rh, respectively. As the CO cannot disrupt the Rh particles at such low temperature, *gem*-dicarbonyl structures cannot be formed, and hence, no twin bands are present, which is in agreement with studies from Primet[16] and Zaki.[33]

Combining the results of these experiments leads to the conclusion that the bands between 2130 and 2000 cm^{-1} originate from two types of *gem*-dicarbonyls, which differ in the way they are bonded to the support.[17–20,32,38,57] One type has its Rh atom attached to an oxygen of the zeolite framework and to a water molecule, denoted as $Rh^{+}(CO)_2-(O_z)(H_2O)$, and the other one has its Rh bonded to two oxygen atoms of the support, $Rh^{+}(CO)_2-(O_z)_2$. The former one exhibits its in-phase and out-of-phase CO stretching bands at 15−25 cm^{-1} higher wavenumbers than the latter one. Furthermore, it can be concluded that CO linearly bonded to metallic Rh, if present, gives rise to a band between 2070 and 2040 cm^{-1}. Finally, the IR data demonstrate as well that the Rh particles must be very small. The prominent bands are due to *gem*-dicarbonyl contributions, and these species are merely formed when the Rh particles are smaller than 1 nm in diameter, whereas particles larger than 2 nm should only give rise to "single" linear and bridge bonded CO bands.[16,19,33,54] This is fully in line with the small Rh−Rh coordination numbers extracted from the EXAFS data and not conflicting with the presence of some larger particles, which appeared on the TEM pictures.

Influence of the Support Composition. As already mentioned in the discussion in Figure 4, the IR spectra of the catalysts vary as a function of the cation introduced in the zeolite material. This is better visualized by Figure 5 where the IR spectra recorded after CO exposure and 30 min vacuum at 323 K are juxtaposed and normalized by their maximum absorbance. Figure 5a shows the $Rh/M^{+}Y$ series, and it is clear that all CO vibration frequencies are red shifting with increasing cation radius, i.e., H < Na < K < Rb < Cs. At the same time, the relative intensities of the absorption bands are changing: the ones of the $Rh^{+}(CO)_2-(O_z)(H_2O)$ carbonyls are decreasing in intensity, whereas those of $Rh^{+}(CO)_2-(O_z)_2$ are more pronounced for the larger cations than for the proton-exchanged support. Additionally, the two bands around 2100 cm^{-1} and the ones around 2030 cm^{-1} get closer to each other when going from Rh/HY to Rh/CsY. In the same way, the spectral differences for the $Rh/M^{2+}Y$ series are presented in Figure 5b. For these catalysts, however, there is not a clear trend. The two bands around 2100 cm^{-1} are equally broad for all samples, but the two extremes (Rh/MgY and Rh/BaY) present broader peaks around 2020−2000 cm^{-1}. A more detailed interpretation is not possible without better insight into the position, shape, and

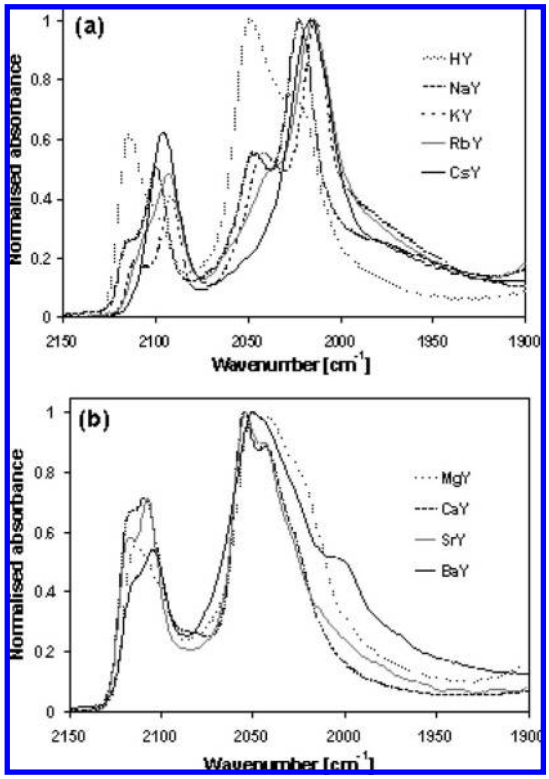

Figure 5. CO IR spectra, normalized to their maximum absorbance, after 30 min exposure to 0.06 bar CO followed by 30 min vacuum at 323 K for (a) the Rh/M^+Y series and (b) the Rh/M^{2+}Y series.

intensity of the different band components. For that reason, peak fitting of the spectra was carried out on the IR spectra recorded after CO exposure and 30 min vacuum. Figure 6 illustrates the results for Rh/NaY, Rh/CsY, Rh/SrY, and Rh/MgY, whereas Table 3 summarizes the maxima obtained for the Rh-adsorbed CO species on all samples. It was found that, next to the water peak at 1640 cm^{-1}, the spectra are best-fitted with four sharp and two or three broad peaks. In continuation to the previous conclusions, the bands at around 2110 and 2050 cm^{-1} can be assigned to the in-phase and out-of-phase CO stretching vibration of the $Rh^+(CO)_2-(O_z)(H_2O)$ species, the bands at around 2100 and 2025 cm^{-1} to the in-phase and out-of-phase CO vibration modes of the $Rh^+(CO)_2-(O_z)_2$ configuration, and the broad peaks at 1995 and 1800 cm^{-1} to CO bridge bonded to oxidized and metallic Rh, respectively. Clear evidence for a band around 2070 cm^{-1} of CO linearly bonded to metallic Rh was not derived from the peak fitting. It should be noted, however, that such a band if present, will largely coincide with the out-of-phase CO stretching band of the $Rh^+(CO)_2$-$(O_z)(H_2O)$ species. Therefore, CO linearly bonded to Rh^0 might as well be present, although in a limited amount.

The curve fitting results confirm that bridge bonded CO on Rh metal exhibits one band for the M^+Y support series and two for the M^{2+}Y ones. It is also evident that the intensity ratio of the *gem*-dicarbonyl CO bands and hence the presence of both species are affected by the promoter cation. However, the mutual intensity ratio of the twin in-phase and out-of-phase vibration bands of the same *gem*-dicarbonyl remains more or less the same. Overall, it averages 0.4 for the $Rh^+(CO)_2-(O_z)_2$ carbonyls bands and 0.3 for the $Rh^+(CO)_2-(O_z)(H_2O)$ ones. The relative integrated band intensities for a *gem*-dicarbonyl species can be used to estimate the angle, α, between the two CO dipoles: $A_{as}/A_{sy} = tg^2(\alpha/2)$.[14,17,42,45,53,56] The application of this formula gives an angle of about 116° for the former species and 123° for the latter one. Miessner and co-workers reported a bond angle of 114° for Rh supported on NaX,[17] while Lefevbre and Ben Taârit calculated an angle of 112° for $Rh^+(CO)_2-(O_z)_2$ and about 90° for $Rh^+(CO)_2-(O_z)(H_2O)$.[38] The former is in good agreement with our results, especially when one takes into account the possible influence of the zeolite structure and composition on the $Rh(CO)_2$ angle.[38] On the contrary, the bond angle that we calculated for $Rh^+(CO)_2-(O_z)(H_2O)$ seems too large. A plausible explanation is an overestimation of the out-of-phase vibration band intensity as result of an underlying contribution of CO linearly bonded to metallic Rh. This phenomenon has also been observed by Hecker and Bell[52] and by Primet.[16]

The CO peak positions of the M^+Y samples series as listed in Table 3, show a clear decrease in wavenumber for the *gem*-dicarbonyl species, when going from the smallest cation (H) to the largest one (Cs). In the M^{2+}Y series, it is not as clear, but overall a trend is present as visualized in Figure 7. The full symbols (◆, ■, ▲ and ●) represent the red shift of the Rh *gem*-dicarbonyls bands compared to the CO gas phase vibration as a function of the cation radius divided by its charge. It can be seen that the red shift increases as a function of the promoter ionic radius to charge ratio. This observation is valid for all linearly bonded CO species resolved in the spectra. In literature, shifts of the carbonyl vibration band as a function of the Rh environment have been attributed to electronic effects and to the back-bonding ability of the metal.[17,24,38] In agreement with our results, Miessner et al. found that the addition of Na to a titania support resulted in a significant shift to lower wavenumbers.[17] Several other observations are relevant to the interpretation of Figure 7. First of all, samples with identical support and different Rh metal dispersions were found to have the same carbonyl IR band positions.[17] Second, a variation in metal loading as high as 0.9 wt % resulted in very small shifts in wavenumber (3 to 5 cm^{-1}).[17] Finally, these CO band positions are independent of the CO coverage.[12,45] We can therefore conclude that the trend in the Rh *gem*-dicarbonyl band positions is due to differences in support composition. A trend in the band position of the bridge bonded species (Table 3) has not been observed. Most likely, this is due to the fact that the effect of the support on the Rh particles is not as large as for isolated Rh cations. Besides, the band originates from several configurations, which can be differently influenced by the cation.

In the discussion of Figures 4 and 6, we already highlighted that the relative intensities of the bands corresponding to linearly bonded CO (i.e., in the form of *gem*-dicarbonyls) and bridge bonded CO seem to depend on the support composition, i.e., the cation present. Furthermore, the intensities of the two bands related to the CO bridge bonded to Rh particles seem to be correlated. When compared to the total absorption intensity, the bridge bonded contributions on metallic Rh (1800 cm^{-1}) and on slightly oxidized Rh (2000 cm^{-1}) are both much larger on the Rh/NaY sample than on catalysts containing more acidic cations (Figure 6). This is further illustrated in Figure 8. The full symbols (▲) represent the relative intensity of the bridge bonded CO-bands as compared to the total IR absorption in the region 2150−1700 cm^{-1} as a function of the support cation Lewis acidity, as expressed by the Kamlet-Taft parameter α.[58] The Lewis acidity of hydrogen is unknown, but its value is supposed to be much higher than for the other cations. It is clear that the relative amount of bridge bonded species is decreasing, and hence, the relative amount of *gem*-carbonyls formed is increasing with increasing Lewis acidity of the promoting cation. This trend can be explained by the fact that more basic cations will push electrons toward the framework oxygen of the support,

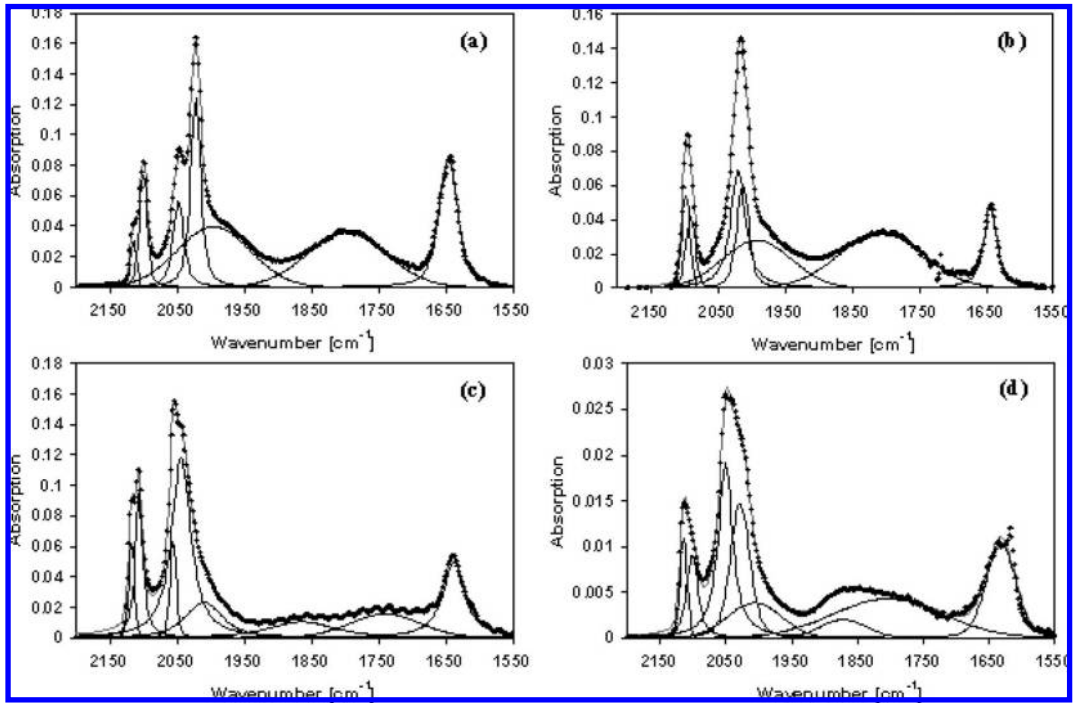

Figure 6. CO IR spectrum after 30 min exposure to 0.06 bar CO and after 30 min vacuum at 323 K on (a) Rh/NaY, (b) Rh/CsY, (c) Rh/SrY, and (d) Rh/MgY with their fitted bands.

TABLE 3: Rh Related Band Positions in the CO IR Spectrum after 30 min Exposure to 0.06 bar CO and 30 min Vacuum at 323 K

	CO band position [cm^{-1}]						
Rh/M^{n+}Y	$Rh^+(CO)_2$ (O_z) (H_2O) (sym)	$Rh^+(CO)_2$ (O_z)$_2$ (sym)	$Rh^+(CO)_2$ (O_z)(H_2O) (as)	$Rh^+(CO)_2$ (O_z)$_2$ (as)	$Rh_n^{\delta+}$-CO	Rh_n^0-CO	
Rh/HY	2114	2100	2049	2025	1990	1843	
Rh/NaY	2114	2100	2048	2022	1995	1797	
Rh/KY	2109	2092	2042	2014	1999	1812	
Rh/RbY	2105	2092	2041	2014	1986	1821	
Rh/CsY	2098	2091	2020	2013	1992	1807	
Rh/MgY	2114	2101	2051	2028	2007	1871	1804
Rh/CaY	2118	2106	2056	2042	2019	1879	1751
Rh/SrY	2118	2106	2056	2043	2010	1864	1740
Rh/BaY	2115	2103	2049	2030	1991	1864	1751

$Rh^+(CO)_2(O_z)(H_2O)$ refers to a Rh *gem*-dicarbonyl species bonded to one oxygen of the zeolite framework and $Rh^+(CO)_2(O_z)_2$ to a Rh *gem*-dicarbonyl species bonded to two oxygens of the support. $Rh_n^{\delta+}-O$ is representing CO in a bridge position on slightly oxidized Rh and Rh_n^0-CO a CO molecule bonded in n-fold bridge position to metallic Rh.

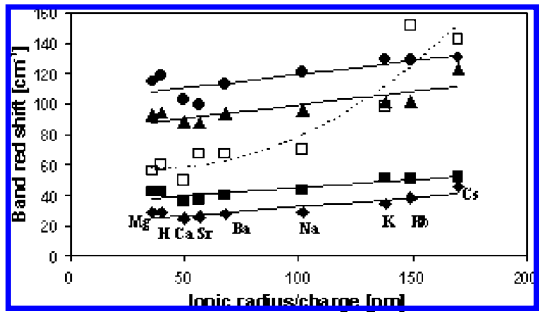

Figure 7. CO IR band red shift versus the CO vibration in the gas phase as a function of the cation ionic radius to charge ratio: for the (◆, ■) in-phase and (▲, ●) out-of-phase stretching vibrations of $Rh^+(CO)_2(O_z)(H_2O)$ and $Rh^+(CO)_2(O_z)_2$ *gem*-dicarbonyls, respectively, and, as a reference, for the (□) Pt-CO linear vibration.[9]

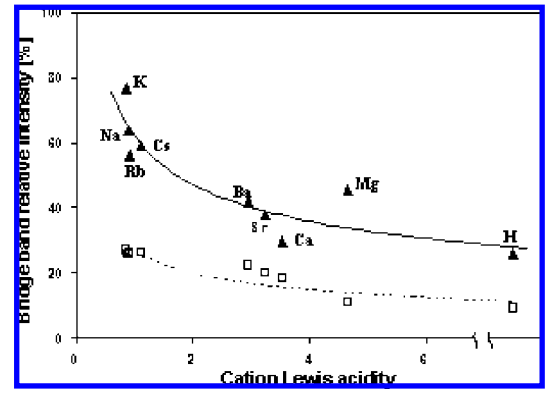

Figure 8. Relative intensity of the bridge bonded CO as compared to the total absorbance of (▲) Rh- and (□) Pt-bonded[9] CO species as a function of the cation Lewis acidity of the support promoter.

which in turn causes the Rh nanoparticles to have a higher electron-density. This gives rise to a larger back-donation to the adsorbed CO π orbitals, thus enhancing the possibility for bridge bond formation. Another interpretation can be made based on the work of Zaki et al., who concluded that the acidity of the support OH groups controls the Rh particle disruption and thus the formation of Rh *gem*-dicarbonyls.[33] In the same

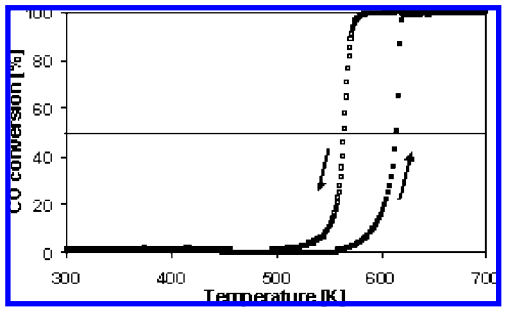

Figure 9. CO conversion as a function of temperature on Rh/CaY upon (■) heating and (□) cooling at a rate of 3 K/min.

way, Iordan and coauthors reported that the addition of K to a Rh/Al_2O_3 catalyst material suppressed the CO-induced Rh particle disruption.[50] It should be noted that the Rh particle size might have an influence on the formation of carbonyls.[16,19,33,54] However, such an impact was not observed due to the fact that the size of the Rh particles is in average smaller than 1.5 nm. Finally, as already mentioned before, the presence of incompletely reduced Rh (i.e., a broadband at 2000 cm^{-1}) might be due to the effect of chlorine residuals,[6,34,35,44] which would affect the trend in Figure 8. This can nevertheless be excluded as the same trend is observed in case the bridge bonded CO's on Rh metal or on slightly oxidized Rh are considered separately and relative to the total intensity of the CO-Rh bands. Moreover, during the reduction process, the changes in the white line intensity of the XANES signal at the K-edge as a function of temperature were very similar. So, differences in reducibility are absent among the samples under study. It can therefore be concluded that the trend observed in Figure 8 is directly linked to the support composition effect through: (1) differences in the electron back-donation capability of the Rh (influencing the amount of bridge bonded CO) and (2) differences in the OH-group acidity of the support (having an impact on the carbonyls formation).

3. CO Oxidation Activity. The CO IR study discussed above shows that the support composition has a clear impact on the electronic properties of supported Rh nanoparticles. It is therefore interesting to correlate these observations with the catalytic activity of the samples in the oxidation of CO. As an example, Figure 9 shows the CO conversion for the fresh Rh/CaY sample in excess of oxygen as a function of temperature upon heating and cooling. The hysteresis seen between the two curves is not uncommon for the CO oxidation reaction. It can be explained by changes in the Rh oxidation state or by differences in CO and O coverage upon heating and cooling.[59–61] This is confirmed by the fact that, upon cycling, the hysteresis remains, but the curves tend to shift to slightly lower temperatures with the cycle number due to sintering of the Rh particles.

The temperature at 50% CO conversion (T_{50}) upon heating up the catalyst powder has been taken as a measure for the catalytic activity. Comparison of the T_{50} values of all catalyst materials under study expressed as the ▲ symbols in Figure 10 shows that this parameter varies for the different samples. It is also clear that T_{50} can be directly correlated to the results of the IR measurements: the catalytic activity increases with decreasing T_{50} and increasing relative intensities of the bridge bonded CO. In principle, the difference in experimental conditions does not allow a direct correlation between the CO species present on the Rh surface during the static CO IR measurements, taken in absence of oxygen, and the catalytic test for the CO oxidation reaction done in large excess of oxygen. However, based on the relation found in the CO IR study between the

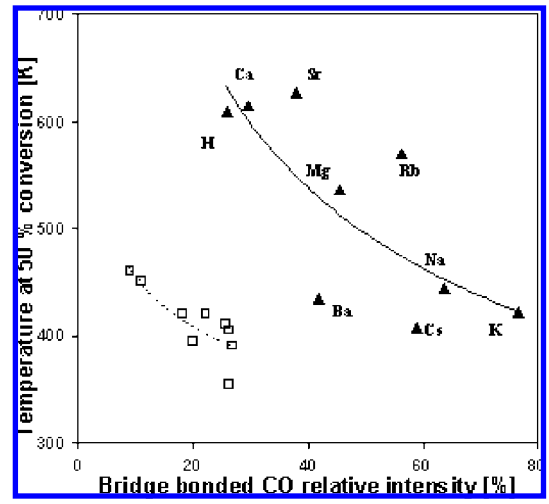

Figure 10. Temperature at 50% conversion for the CO oxidation reaction as a function of the relative CO IR absorption intensity of the bridge bonded CO (▲) on Rh and (□) on Pt.[9]

relative amount of bridge species and the Lewis acidity of the promoting cation, it can be concluded that the formation of bridge bonded species is directly linked to the electron-density of the Rh catalyst. This has a direct influence on its catalytic activity. These results are in agreement with the studies of Anderson[51] and Dent et al.,[48] who reported that carbonyl species have low activity in the CO oxidation and CO/NO reactions, respectively. The former author added that at high O_2/CO ratios small clusters were formed with bridge adsorption sites. They also agree with the work of Iordan and coauthors, who found that the addition of K to Rh/Al_2O_3 catalysts promoted the CO decomposition as the result of an enriched electron density of the Rh metal active sites.[50] Moreover, Miessner et al. reported a direct relation between the IR data and the Rh activity in the CO hydrogenation reaction, but did not compare it to the bridge bonded CO.[17] Finally, the presence of chlorine might have some impact on the Rh catalytic activity, especially at low temperature.[6,34,35,45,62] However, EXAFS, XANES and CO IR data analysis revealed that its impact, if any, is both small and likely to be about the same upon all samples.

4. Comparison between the Chemistry of Supported Pt and Rh Nanoparticles. To determine whether the promoting effect of the different cations on the Rh catalysts is similar to what we observed on the corresponding $Pt/M^{+}Y$ and $Pt/M^{2+}Y$ samples,[9] we compared the results of both studies. For that purpose, we added the data of the Pt-catalysts to Figures 7, 8, and 10 (□ symbols). In Figure 7, the red shifts of the Rh *gem*-dicarbonyl bands as a function of the radius-to-charge ratio of the promoting cation (◆, ■, and ▲) are compared to the ones of the linearly bonded CO on Pt (□). Obviously, it would have been more logical to compare these data to CO linearly bonded to Rh, but as explained previously, it was not possible to extract this band from the spectra. . It is nevertheless clear that the red shift is increasing with increasing cation radius-to-charge ratio for both noble metal catalysts. At first glance, the more pronounced effect for the Pt series seems to contradict intuition, in view of the isolated Rh atoms as opposed to the larger Pt particles. There are, however, some fundamental differences. First, the Rh might be less sensitive to the support, because the bands under consideration originate from Rh in a +1 oxidation state whereas Pt is metallic. This means there are less electrons available for back-donation to CO from the Rh. Second, the Rh *gem*-dicarbonyl species undergo some constraints because the Rh cation is directly bonded to the zeolite matrix.[39]

Figure 8 represents the relative intensity of the bridge-bonded CO band as compared to the total absorption of Rh and Pt metal-bonded CO species as a function of the cation Lewis acidity. The trends for both Rh (▲) and Pt (□) are again similar but this time, the differences in the Rh series are more pronounced. This disparity may be caused by the intervention of two parameters in the case of Rh, i.e., electron density on the metal and acidity of the support, instead of one in the case of Pt, i.e., electron density.

Figure 10 shows the temperature at 50% CO conversion under large excess of oxygen as a function of the relative intensity of the bridge bonded CO in the static CO IR measurements. Although the data points of the Rh catalyst series are more scattered and the influence of the cation is larger for Rh than for Pt, the trend is once more equivalent for both noble metals.

Conclusions

The following conclusions can be drawn from this work:

1. Exposure of zeolite-supported Rh nanoparticles to CO gives rise to more complex IR spectra then for zeolite-supported Pt nanoparticles.

2. This increased complexity is due to the fact that CO modifies the state of the supported Rh particles upon adsorption, the smallest particles being disrupted into isolated Rh cations giving rise to Rh *gem*-dicarbonyl species.

3. $Rh^{+}(CO)_2$ species exhibit typical narrow IR bands, which are sensitive to the support composition. This is demonstrated by ion exchanging the zeolite with different monovalent and divalent cations. It was observed that the IR red shift, as compared to the vibration frequency of CO in the gas phase increases with increasing ionic radius to charge ratio of the promotor. The same trend, but to a larger extent, was also observed for zeolite-based Pt particles.

4. The relative intensity of the bridge bonded CO as referred to the total absorbance of the Rh-bonded CO species, decreases with increasing Lewis acidity of the promoting cation. This is similar to what has been observed on zeolite Y-supported Pt nanoparticles with alkali and alkali-earth promoters. However, the differences are more pronounced for the Rh catalysts, due to the larger contribution of bridge bonded CO in these samples.

5. This last trend is directly correlated to the Rh catalytic activity for the CO oxidation reaction, since the temperature at 50% CO conversion is lower for larger relative intensities of the bridge bonded CO. Again, the differences are more pronounced for the zeolite Y-supported Rh catalysts as compared to the Pt.

Acknowledgment. The authors acknowledge Toyota Motor Europe for financial support and beamtime grants from DUBBLE in Grenoble. We also thank Mr. Takagi from Toyota Motor Corporation for the ICP AES measurements and Mr. van der Spek from Utrecht University for the HRTEM pictures. Finally, Prof. Matsumoto from Toyota Motor Corporation and Dr. Nagai, Dr. Dohmae, and Dr. Shinjoh from Toyota R&D Central Laboratory are thanked for fruitful discussions.

References and Notes

(1) (a) Davis, M. E.; Rode, E.; Taylor, D.; Hanson, B. E. *J. Catal.* **1984**, *86*, 67–74. (b) Atsushi, A.; Rao, L.-F.; Kosugi, N.; Kuroda, H.; Ichikawa, M. *Appl. Catal.* **1989**, *50*, 295–301.

(2) (a) Weber, W. A.; Gates, B. C. *J. Catal.* **1998**, *180*, 207–217. (b) Boutros, M.; Launay, F.; Nowicki, A.; Onfroy, T.; Herledan-Semmer, V.; Roucoux, A.; Gédéon, A. *J. Mol. Catal. A: Chem.* **2006**, *259*, 91–98. (c) Lee, T. J.; Gates, B. C. *J. Mol. Catal.* **1992**, *71*, 335–346. (d) Bando, K. K.; Soga, K.; Kunimori, K.; Ichikuni, N.; Okabe, K.; Kusama, H.; Sayama, K.; Arakawa, H. *Appl. Catal. A: Gen.* **1998**, *173*, 47–60. (e) Bando, K. K.; Soga, K.; Kunimori, K.; Arakawa, H. *Appl. Catal. A: Gen.* **1998**, *175*, 67–81. (f) Bando, K. K.; Ichikuni, N.; Soga, K.; Kunimori, K.; Arakawa, H.; Asakura, K. *J. Catal.* **2000**, *194*, 91–104.

(3) (a) Denley, D. R.; Raymond, R. H.; Tang, S. C. *J. Catal.* **1984**, *87*, 414–423. (b) Andersson, S. L. T. *J. Catal.* **1981**, *71*, 233–243. (c) Bódis, J.; Zsakó, J.; Németh, C.; Mink, J. *Vib. Spectrosc.* **1995**, *9*, 197–202.

(4) (a) Siri, G. J.; Guerrero-Ruiz, A.; Rodriguez-Ramos, I.; Terreros, P. *Appl. Catal. A: Gen.* **1993**, *107*, 59–71. (b) Treviño, H.; Hyeon, T.; Sachtler, W. M. H. *J. Catal.* **1997**, *170*, 236–243. (c) Xua, B.-Q.; Suna, K.-Q.; Zhua, Q.-M.; Sachtler, W. M. H. *Catal. Today* **2000**, *63*, 453–460.

(5) (a) Gandhi, H. S.; Graham, G. W.; McCabe, R. W. *J. Catal.* **2003**, *216*, 433–442. (b) Taylor, K. C.; Schlatter, J. C. *J. Catal.* **1980**, *63*, 53–71. (c) Taylor, K. C. *Catal. Rev.-Sci. Eng.* **1993**, *35*, 457–481.

(6) Fontaine, C.; Krafft, J.-M.; Thomas, C.; Djéga-Mariadassou, G. *Phys. Chem. Chem. Phys.* **2006**, *8*, 3732–3740.

(7) Manuel, I.; Chaubet, J.; Thomas, C.; Colas, H.; Matthess, N.; Djéga-Mariadassou, G. *J. Catal.* **2004**, *224*, 269–277.

(8) Yu Yao, Y.-F. *J. Catal.* **1984**, *87*, 152–162.

(9) Visser, T.; Nijhuis, T. A.; Van der Eerden, A. M. J.; Jenken, K.; Ji, Y.; Bras, W.; Nikitenko, S.; Ikeda, Y.; Lepage, M.; Weckhuysen, B. M. *J. Phys. Chem. B* **2005**, *109*, 3822–3831.

(10) Van der Eerden, A. M. J.; Visser, T.; Nijhuis, T. A.; Ikeda, Y.; Lepage, M.; Koningsberger, D. C.; Weckhuysen, B. M. *J. Am. Chem. Soc.* **2005**, *127*, 3272–3273.

(11) Lepage, M.; Visser, T.; van der Eerden, A. M. J.; Soulimani, F.; Weckhuysen, B. M. *Vib. Spectrosc.* **2008**, doi:10.1016/j.vibspec.2007.11.006.

(12) Yang, A. C.; Garland, C. W. *J. Phys. Chem.* **1957**, *61*, 1504–1512.

(13) Yates, D. J. C.; Murrell, L. L.; Prestridge, E. B. *J. Catal.* **1979**, *57*, 41–63.

(14) Ivanova, E.; Mihaylov, M.; Thibault-Starzyk, F.; Daturi, M.; Hadjiivanov, K. *J. Catal.* **2005**, *236*, 168–171.

(15) Chafik, T.; Kondarides, D. I.; Verykios, X. E. *J. Catal.* **2000**, *190*, 446–459.

(16) Primet, M. *J. Chem. Soc. Farad. Trans. 1* **1978**, *74*, 2570–2580.

(17) Miessner, H.; Gutschick, D.; Ewald, H.; Müller, H. *J. Mol. Catal.* **1986**, *36*, 359–373.

(18) Shannon, R. D.; Vedrine, J. C.; Naccache, C.; Lefebvre, F. *J. Catal.* **1984**, *88*, 431–447.

(19) Bergeret, G.; Gallezot, P.; Gélin, P.; Ben Taârit, Y.; Lefebvre, F.; Naccache, C.; Shannon, R. D. *J. Catal.* **1987**, *104*, 279–287.

(20) Tomczak, D. C.; Lei, G. D.; Schünemann, V.; Treviño, H.; Sachtler, W. M. H. *Micropor. Mater.* **1996**, *5*, 263–278.

(21) Vaarkamp, M.; Linders, J. C.; Koningsberger, D. C. *Physica B* **1995**, *208/209*, 159–160.

(22) Koningsberger, D. C.; Mojet, B. L.; van Dorssen, G. E.; Ramaker, D. E. *Top. Catal.* **2000**, *10*, 143–155.

(23) Gijzeman, O. L. J.; Mens, A. J. M.; Van Lenthe, J. H.; Mortier, W. J.; Weckhuysen, B. M. *J. Phys. Chem. B* **2003**, *107*, 678–684.

(24) Kamble, V. S.; Gupta, N. M.; Kartha, V. B.; Iyer, R. M. *J. Chem. Soc. Faraday Trans.* **1993**, *89*, 1143–1150.

(25) Zhang, Y.; Toebes, M. L.; Van der Eerden, A.; O'Grady, W. E.; de Jong, K. P.; Koningsberger, D. C. *J. Phys. Chem. B* **2004**, *108*, 18509–18519.

(26) Newton, M. A.; Dent, A. J.; Diaz-Moreno, S.; Fiddy, S. G.; Jyoti, B.; Evans, J. *Chem. Eur. J.* **2006**, *12*, 1975–1985.

(27) Jentys, A. *Phys. Chem. Chem. Phys.* **1999**, *1*, 4059–4063.

(28) van Zon, J. B. A. D.; Koningsberger, D. C.; van'tBlik, H. F. J.; Sayers, D. E. *J. Chem. Phys.* **1985**, *82*, 5742–5754.

(29) Gloor, A. P.; Prins, R. *J. Phys. Chem.* **1994**, *98*, 9865–9873.

(30) van't Blik, H. F. J.; van Zon, J. B. A. D.; Huizinga, T.; Vis, J. C.; Koningsberger, D. C.; Prins, R. *J. Am. Chem. Soc.* **1985**, *107*, 3139–3147.

(31) Martinez-Arias, A.; Soria, J.; Conesa, J. C. *J. Catal.* **1997**, *168*, 364–373.

(32) Wong, T. T. T.; Stakheev, A. Y.; Sachtler, W. M. H. *J. Phys. Chem.* **1992**, *96*, 7733–7740.

(33) Zaki, M. I.; Tesche, B.; Kraus, L.; Knözinger, H. *Surf. Interface Anal.* **1988**, *12*, 239–246.

(34) Force, C.; Belzunegui, J. P.; Sanz, J.; Martínez-Arias, A.; Soria, J. *J. Catal.* **2001**, *197*, 192–199.

(35) Newton, M. A.; Jyoti, B.; Dent, A. J.; Fiddy, S. G.; Evans, J. *Chem. Commun.* **2004**, 2382–2383.

(36) Oudenhuijzen, M. K.; Van Bokhoven, J. A.; Miller, J. T.; Ramaker, D. E.; Koningsberger, D. C. *J. Am. Chem. Soc.* **2004**, *127*, 1530–1540.

(37) Newton, M. A.; Dent, A. J.; Diaz-Moreno, S.; Fiddy, S. G.; Evans, J. *Angew. Chem., Int. Ed.* **2002**, *41*, 2587–2589.

(38) Lefevbre, F.; Ben Taârit, Y. *Nouv. J. Chim.* **1984**, *8*, 387–391.

(39) Martra, G.; Ocule, R.; Marchese, L.; Centi, G.; Coluccia, S. *Catal. Today* **2002**, *73*, 83–93.

(40) Rakic, V. M.; Hercigonja, R. V.; Dondur, V. T. *Micropor. Mesopor. Mat.* **1999**, *27*, 27–39.

(41) Klepel, O.; Hunger, B. *J. Therm. Anal. Calorim.* **2005**, *80*, 201–206.

(42) Yagi, F.; Tsuji, H.; Hattori, H. *Microporous Mater.* **1997**, *9*, 237–245.
(43) Lavalley, J. C.; Saussey, J.; Lamotte, J.; Breault, R.; Hindermann, J. P.; Kiennemann, A. *J. Phys. Chem.* **1990**, *94*, 5941–5947.
(44) Trautmann, S.; Baerns, M. *J. Catal.* **1994**, *150*, 335–344.
(45) Rice, C. A.; Worley, S. D.; Curtis, C. W.; Guin, J. A.; Tarrer, A. R. *J. Chem. Phys.* **1981**, *74*, 6487–6497.
(46) Almusaiteer, K. A.; Chuang, S. S. C. *J. Phys. Chem. B* **2000**, *104*, 2265–2272.
(47) Kusama, H.; Bando, K. K.; Okabe, K.; Arakawa, H. *Appl. Catal. A: Gen.* **2001**, *205*, 285–294.
(48) Dent, A. J.; Evans, J.; Fiddy, S. G.; Jyoti, B.; Newton, M. A.; Tromp, M. *Angew. Chem., Int. Ed.* **2007**, *46*, 5356–5358.
(49) Dujardin, C.; Mamede, A.-S.; Payen, E.; Sombret, B.; Huvenne, J. P.; Granger, P. *Top. Catal.* **2004**, *30/31*, 347–352.
(50) Iordan, A.; Zaki, L. I.; Kappenstein, C.; Géron, C. *Phys. Chem. Chem. Phys.* **2003**, *5*, 1708–1715.
(51) Anderson, J. A. *J. Chem. Soc. Faraday Trans.* **1991**, *87*, 3907–3911.
(52) Hecker, W. C.; Bell, A. T. *J. Catal.* **1983**, *84*, 200–215.
(53) Miessner, H.; Burkhardt, I.; Gutschick, D.; Zecchina, A.; Morterra, C.; Spoto, G. *J. Chem. Soc. Faraday Trans. 1* **1989**, *85*, 2113–2126.
(54) van′t Blik, H. F. J.; van Zon, J. B. A. D.; Huizinga, T.; Vis, J. C.; Koningsberger, D. C.; Prins, R. *J. Phys. Chem.* **1983**, *87*, 2264–2267.
(55) Burkhardt, I.; Gutschick, D.; Lohse, U.; Miessner, H. *J. Chem. Soc. Chem. Comm.* **1987**, 291–292.
(56) Vayssilov, G. N.; Rösch, N. *J. Am. Chem. Soc.* **2002**, *124*, 3783–3786.
(57) Gélin, P.; Dutel, J.-F.; Ben Taârit, Y. *J. Chem. Soc. Chem. Comm.* **1990**, 1746–1747.
(58) Marcus, Y. *Ion Properties*; Marcel Dekker:New York, 1997, p 193.
(59) Makeev, A. G.; Slinko, M. M.; Janssen, N. M. H.; Cobden, P. D.; Nieuwenhuys, B. E. *J. Chem. Phys.* **1996**, *105*, 7210–7222.
(60) Hrncír, T.; Nahasil, V. *Surf. Sci.* **2002**, *507−510*, 859–864.
(61) Ioannides, T.; Efstathiou, A. M.; Zhang, Z. L.; Verykios, X. E. *J. Catal.* **1995**, *156*, 265–272.
(62) Fontaine-Gautrelet, C.; Krafft, J.-M.; Djéga-Mariadassou, G.; Thomas, C. *J. Catal.* **2007**, *247*, 34–42.

JP711743G